

Over-resolution in map-making based on accurate instrument model and regularized inversion. Application to SPIRE/Herschel.

F. Orieux¹, J.-F. Giovannelli^{1,2}, T. Rodet¹, A. Abergel³, H. Ayasso³, and M. Husson³

¹ Laboratoire des Signaux et Systèmes (CNRS – Supélec – Univ. Paris-Sud 11), Plateau de Moulon, 91 192 Gif-sur-Yvette, France. e-mail: orieux, rodet@lss.supelec.fr

² Laboratoire de l'Intégration du Matériau au Système (CNRS – Univ. Bordeaux 1 – IPB), 33 405 Talence, France. e-mail: Giova@IMS-Bordeaux.fr

³ Institut d'Astrophysique Spatiale (CNRS – Univ. Paris-Sud 11), 91 405 Orsay, France. e-mail: abergel@ias.u-psud.fr

Submitted March, 2011

Abstract — This article concerns over-resolution methods for image reconstruction from data provided by a family of scanning instruments like the Herschel observatory. The work is centered on building a model of the instrument that faithfully reflects the physical reality, accurately taking the acquisition process into account so as to explain the data in a reliable manner. The inversion, i.e. the image reconstruction process, is based on a linear approach resulting from a quadratic regularized criterion and numerical optimization tools. The inversion process produces maps that are over-resolved with respect to the nominal resolution of the instrument. The application concerns the reconstruction of maps for the SPIRE instrument of the Herschel observatory. The numerical evaluation uses simulated and real data to compare the standard tool (coaddition) and the proposed method. We demonstrate a capacity to restore spatial frequencies over a bandwidth four times that possible with coaddition and thus to correctly show details invisible on standard maps. The proposed approach is also applied to real data with significant improvement in spatial resolution.

Key words. Techniques: image processing, data acquisition modelling, inverse problem, deconvolution, over-resolution, regularization, image processing. Methods: statistical, numerical. Astronomical instrumentation, methods and techniques

1. Introduction

Map making is a critical step in the processing of astronomical data from various imaging instruments (interferometers, telescopes, spectro-imager...). A very large number of papers have been devoted to this question in

Send offprint requests to: F. Orieux

various literature and two recent special issues have been published [Leshem et al., 2010, 2008] in the signal-image processing literature. Since the observed sky may contain structures of various scales, from extended emission to point sources, the challenge is to design reconstruction method delivering maps that are photometrically valid for the broadest range of spatial frequencies.

For long-wavelength instruments, be they ground based (SCUBA/JCMT, LABOCA/APEX, . . .), on-board balloons (Archeops, BLAST, . . .) or space borne (IRAS, ISO, Spitzer, WMAP, Planck, Herschel, . . .), the task is especially challenging for two reasons. First, the resolution is poor at such wavelength. Second, the number of detectors in the focal plane of such instruments is limited, so, it is generally not fully sampled. Therefore, specific scanning strategies have to be defined, depending on the detector positions, and closely combined with a well designed image reconstruction method.

The Herschel Space Observatory [Pilbratt et al., 2010] was launched in May 2009 together with the Planck satellite. It continuously covers the 55–672 μm spectral range with its very high resolution spectrometer HIFI [de Graauw et al., 2010] and its two photometers / medium resolution spectrometers PACS [Poglitsch et al., 2010] and SPIRE [Griffin et al., 2010]. With a 3.5 m primary mirror, Herschel is the largest space telescope launched to date. In order to take full advantage of the size of the telescope, the accurate representation and processing of the highest spatial frequencies presents a particular challenge. To this end, two step-by-step photometer pipelines have been developed by the instrument consortia by Griffin et al. [2008] for SPIRE and by Wieprecht et al. [2009] for PACS: they produce flux density timelines corrected for various effects, calibrated and associated with sky coordinates (Level-1 products), then produce maps (Level-2 products). An important step is the correction of the $1/f$ noise components, which can be correlated or uncorrelated between bolometers. For SPIRE, a significant fraction of the correlated component is processed using the signals delivered by blind bolometers. For PACS, it is currently processed using different kinds of filtering. The glitches due to the deposit of thermal energy by ionizing cosmic radiation are flagged or corrected. Finally, the output can be simply coadded to produce “naive maps”. Maximum likelihood approaches, namely MADmap [Cantalupo et al., 2010] and SANEPIC [Patanchon et al., 2008], have also been developed to compute maps, using the spatial redundancy to correct for the $1/f$ noise.

There are several drawbacks to these pipelines. First, as they work on a step-by-step basis, the global process suffers from the limitation of the worst step. Second, the information available in one step is not fully exploited by the others since only the final result of one step is handed over to the following. Third, the instruments and the telescope properties (mainly the diffraction) are not taken into account, so, the maps are unavoidably smoothed by the PSF, whereas the scanning strategy allows higher spatial frequencies to be indirectly observed.

In order to overcome these limitations, we resort to an inverse problem approach [Idier, 2008] that is founded on an instrument model and an inversion method.

- It requires an instrument model that faithfully reflects the physical reality so as to distinguish, in the observations, between what is caused by the instrument and what is due to the actual sky. To this end, an important contribution of our paper is an analytical model based on a physical description of the phenomena, as functions of continuous variables. Moreover, it includes scanning strategy, mirror, wavelength filter, feedhorns, bolometers and read-out electronics. As far as the resolution is concerned, the point is the following. On the one hand, the field of view is covered by hexagonally packed feedhorn-coupled bolometers, and the distance between

adjacent bolometers is twice the PSF width, resulting in spectral aliasing. On the other hand, the scanning strategy introduces spatial redundancies contributing to a higher equivalent sampling frequency. So, it is crucial to properly take into account the scanning strategy and the whole instrument including aliasing in order to obtain over-resolution and reverse aliasing (see also the analysis of [Orieux et al., 2009]). To the best of our knowledge, such a model has never been used in a map making method.

- The inversion step constitutes an ill-posed problem [Idier, 2008] due to the deficit of available information, and the ill-posedness becomes all the more marked as resolution requirement increases. The inversion methods must therefore include other information in order to compensate for the deficits in the observations. Each reconstruction method is thus specialized for a certain class of maps (point sources, diffuse emission, superposition of the two...) according to the information taken into account. From this standpoint, the present paper is essentially devoted to extended emission.

From the methodological point of view, the used inversion comes within the framework linear regularized method [Tikhonov & Arsenin, 1977; Andrews & Hunt, 1977]. It relies on a quadratic criterion involving an adequation measure (observed data vs model output) and a spatial smoothness measure. From a practical standpoint, we resort to a gradient based optimisation algorithm [Nocedal & Wright, 2000] to compute the map.

Moreover, in as much as it relies on two sources of information, the method is based on a trade-off tuned by means of an hyperparameter. It is empirically set in the present paper and work in progress, inspired from [Orieux et al., 2010], is devoted to the question of the hyperparameter and instrument parameters auto-calibration (myopic and unsupervised inversion).

One of the most striking results of the present paper is the correct restoration of small-scale structures (wide band) whereas they are not detectable on naive maps. Such a result is reached thanks to the developed instrument model together with the used inversion: they jointly enable the proposed method to reduce instrument effects, overtake instrument limitations and restore high spatial frequencies. The latter point is closely related to the capability to reverse aliasing in an inversion process.

In the image processing community, such capabilities are referred to as super-resolution [Park et al., 2003]. A lot of work has been devoted to this topic and the proposed paper is partly inspired by recent developments in this field. They are usually based on various (scene or camera) motion or scanning strategy. Some of them account for possible rotation [Elad & Feuer, 1999] and/or a magnifying factor [Rocheffort et al., 2006]. Other approaches introduce edge-preserving prior [Nguyen et al., 2001; Woods et al., 2006]. These works rely on the description of the unknown object as a function of continuous variables, that is decomposed on pixel indicator basis [Hardie et al., 1997; Patti et al., 1997], on a truncated discrete Fourier basis [Vandewalle et al., 2007], on a family of regularly shifted Gaussian functions [Rodet et al., 2008], or spline family [Rocheffort et al., 2006]. Other approaches have been proposed, based on shift-and-add step [Farsiu et al., 2004] followed by a deconvolution step [Molina & Ripley, 1989]. Finally, several contributions are devoted to the performance of super-resolution approaches [Champagnat et al., 2009; Orieux et al., 2009].

This paper is organized as follows. The instrument model describing the relationship between the measured data and the unknown sky is presented in Section 2. Section 3 details the method which is proposed to inverse the

data and compute high resolution maps. Finally, Section 4 presents experimental results, first on simulated data (Section 4.1) then on real data (Section 4.2).

2. Instrument model

The prime objective of the instrument model is to reproduce the data for a fixed sky by describing the physics of the acquisition. The sky, $\mathcal{X}(\alpha, \beta, \lambda)$, is characterized by two spatial dimensions (α, β) and one spectral dimension λ . The closer the description of the acquisition is to reality, the better the inversion method is able to distinguish between information coming from the object and changes introduced by the instrument.

The principle of faithfully representing the real world is difficult to conciliate with the practical constraints of numerical computing. In general, the reconstruction algorithms call on the instrument model many times in order to reproduce a data set resulting from a current sky. This is one of the differences with a simulator [Sibthorpe et al., 2009; Sibthorpe & Griffin, 2006] which is designed to be run once per data set and is not included in a reconstruction algorithm. It is thus necessary to make choices or approximations to reduce computation time.

2.1. Physical models

2.1.1. Mode of observation

To model telescope translations, we use a frame of reference defined by the instrument. The map present at the input is time dependent and can be written

$$\mathcal{X}(\alpha, \beta, \lambda, t) = \mathcal{X}(\alpha - p_\alpha(t), \beta - p_\beta(t), \lambda), \quad (1)$$

where α and β define the central angular position of the observation and $(p_\alpha(t), p_\beta(t))$ the translations in the two directions as a function of time t .

Here, we present only the *Large map* protocol for wide field of view. Data are acquired over a complete observation sequence composed of two practically perpendicular directions and several scans in one sense and the other for each of the two directions. The pointing acceleration and deceleration phases are outside the zone of interest and there is no rotation during the observation sequence. The pointing functions are thus written

$$p_\alpha(t) = v_\alpha t + c_\alpha \quad \text{and} \quad p_\beta(t) = v_\beta t + c_\beta \quad (2)$$

for scanning at a constant velocity (v_α, v_β) . The pointing accuracy is of the order of a few seconds of arc. This protocol enables spatial redundancy to be introduced, which is an essential element for the reconstruction of a sky at a resolution greater than the focal plane resolution (without scanning) [Orieux et al., 2009; Champagnat et al., 2009].

2.1.2. Optics

The Herschel Telescope is a classical Cassegrain instrument with a 3.5 m diameter primary mirror and a 308 mm diameter secondary mirror. The SPIRE photometer has three channels for a single field of view. The light is split by a combination of dichroics and flat folding mirrors. The spectral channels are defined by a sequence of metal

mesh filters and the reflection/transmission edges of the dichroics. They are centred at approximately 250, 350 and 500 μm (noted as PSW, PMW and PLW respectively). We take the overall transmission curves of the wavelength filter $h_k(\lambda)$, for $k = 1, 2, 3$, as given by the SPIRE Observers' Manual (no analytical form is available).

The three detector arrays contain 139 (250 μm), 88 (350 μm) and 43 (500 μm) bolometers, each coupled to the telescope beam with hexagonally close-packed circular feedhorns. The beam solid angle is apodized by a bell-shaped weight whose width increases with λ . Efforts have been made to correctly integrate the feedhorns in the instrument model but the detailed coupling of feedhorns on incoming radiation is, to the best of our knowledge [Griffin et al., 2002], not fully understood at present.

Our final choice as an effective PSF for the telescope coupled with feedhorns is a Gaussian shape $h_o(\alpha, \beta, \lambda)$. This choice has two advantages: (i) it allows a closed equation for the instrument model (see Sec. 2.2), and (ii) it is in adequation with the global response measured from observations of Neptune (Griffin et al. 2010). As a first approach, we take isotropic Gaussians with standard deviations $\sigma_o(\lambda) = c\lambda$ proportional to the wavelength since the width of the beam varies almost linearly with the wavelength. The coefficient of proportionality c is obtained by a least square fit of the Gaussian FWHM with the measured FWHM in [Ferlet, 2007]. The widths obtained are close to the FWHM measured on the sky with 18.1'', 25.2'', and 36.9'' at 250 μm , 350 μm and 500 μm , respectively (Griffin et al. 2010). The feedhorn diameter is $2F\lambda$, which introduces a focal plane sampling period of $2F\lambda$ (50'' for the 350 nm array), or equivalently with sampling frequency $f_s \approx 0.02 \text{ arcsecond}^{-1}$.

The output after each feedhorn is then written as a 2D convolution of the input $\mathcal{X}(\alpha, \beta, \lambda, t)$ and the effective PSF h_o in addition to the h_k wavelength filter

$$\mathcal{X}_c^{lm}(\lambda, t) = h_k(\lambda) \iint \mathcal{X}(\alpha, \beta, \lambda, t) h_o(\alpha - \alpha_{lm}, \beta - \beta_{lm}, \lambda) d\alpha d\beta \quad (3)$$

where $(\alpha_{lm}, \beta_{lm})$ is the direction pointed by the feedhorn (l, m) , for $l = 1, \dots, L$ and $m = 1, \dots, M$. Finally, the optics is modelled as a linear invariant system w.r.t. continuous variable.

2.1.3. Bolometers

To set up the bolometer model, we took the thermal model of [Sudiwala et al., 2002], which was also used in the simulator developed by [Sibthorpe et al., 2009]. Bolometers absorb all the received radiation

$$P^{lm}(t) = \int_{\lambda} \mathcal{X}_c^{lm}(\lambda, t) d\lambda \quad (4)$$

and this power provides the system excitation. The temperature $T^{lm}(t)$ constitutes the system output to be determined. The link between the input $P(t)$ and the response $T(t)$ is described by the differential equation deduced from a thermal balance,

$$C \frac{dT}{dt} - \frac{R(T)V_p^2}{R_c^2} + \frac{G_0}{T_0^\nu(\nu+1)} (T^{\nu+1} - T_0^{\nu+1}) = P$$

where C is the heat capacity of the bolometer, $R(T)$ is its resistivity, T_0 is the temperature of the thermal bath, ν is a physical parameter that depends on the bolometer, G_0 is the thermal conductance (at temperature T_0) and V_p and R_c are the polarization voltage and charge. No explicit solution of this equation is available in the literature. Sudiwala's approach [Sudiwala et al., 2002], adopted here, is to linearize this equation around an operating point (\bar{T}, \bar{P}) . In the following, we consider only the variable part of the flux and the constant part that defines the operating point is not included in the expressions. All the constants are defined with respect to the operating point.

For SPIRE, most of the observations should be carried out in the linear regime [Griffin, 2006, 2007]. We thus consider that a first-order development is sufficient to model the bolometer behaviour correctly. Then, knowing how the resistivity $R(T)$ varies with temperature, it is possible to determine the tension at the terminals. This first-order development models the bolometer as a first-order, low-pass linear invariant system having an impulse response

$$h_b(t) = S \exp[-t/\tau] \quad (5)$$

where the gain S and the time constant τ depend on the physical parameters in the differential equation [Sudiwala et al., 2002]. The values of these parameters are defined with respect to the operating point and correspond to the official SPIRE characteristics [Griffin, 2006, 2007]. The output voltage around the operating point can then be written as a function of the incident flux:

$$y_{lm}(t) = \int_{t'} \int_{\lambda} \mathcal{X}_c^{lm}(\lambda, t') h_b(t' - t) dt' d\lambda. \quad (6)$$

Finally, downstream, we have the read-out electronics, composed of several stages (modulation, amplification, low-pass filter, demodulation, quantification). However, except for the low-pass filters, they seem to have negligible effects relative to the other elements and are not taken into consideration in our model. The equations are nevertheless available [Griffin, 2007] and it is possible to integrate them into the model.

About the low-pass filters, they introduce a delay on the data with respect to the telescope position along the scan. As a trade-off between model accuracy and computation time, we have chosen to model the combination of the low-pass filter and the bolometer as a global first-order filter. The time constant¹ value (0.2 s) is taken to be representative of the combination.

Finally we take into account regular time sampling that takes the values at times $t = nT_s$ (with a sampling frequency $F_s = 1/T_s \approx 30$ Hz) and then $y_{lm}^n = y_{lm}(nT_s)$, for $n = 1, \dots, N$.

2.1.4. Complete equation of model

Putting the above elements end to end gives the equation of the acquisition chain. For a spectral channel k , the time signal at the bolometer (l, m) at time n is written

$$y_{lm}^n = \iint h_k(\lambda) \iint \mathcal{X}(\alpha - p_\alpha(t), \beta - p_\beta(t), \lambda) h_o(\alpha - \alpha_{lm}, \beta - \beta_{lm}, \lambda) d\alpha d\beta h_b(nT_s - t) d\lambda dt. \quad (7)$$

This equation brings in four integrals: two coming from the optics (spatial convolution), one from the spectral integration and one from the time convolution. This is the fundamental equation of the instrument model since it describes the data y_{lm}^n bolometer by bolometer and at every instant as a function of the sky $\mathcal{X}(\alpha, \beta, \lambda)$. It should be noted that this model includes the discretization process in the sense that the data y_{lm}^n are functions of discrete variables (l, m, n) and the sky \mathcal{X} is a function of continuous variables (α, β, λ) .

¹ Eventually, as for the illustration on real data Section 4.2, the correction of the low-pass filter can be performed using the Herschel Interactive Processing Environment (HIPE), and the time constant of the first-order low-pass filter is set to the time constant for the bolometer alone (5.7 ms).

2.1.5. Model of sky for over-resolution

The model of the sky is an important element for the reconstruction. As stated in the introduction and presented in Section 2.1.1, the spatial redundancy of the data should allow for partial reverse aliasing and enable a over-resolved sky to be estimated [Orieux et al., 2009]. The description of \mathcal{X} must therefore be suitable for over-resolved reconstruction and, in particular, allow a fine description of the physical reality in connection with the above instrument model.

Firstly, unlike conventional models [Sibthorpe et al., 2009; Cantalupo et al., 2010], we take into account the spectral variations of the sky within each channel. The emission observed by SPIRE is mainly due to dust particles in thermal equilibrium (between emission and absorption of UV and visible photons from incident radiation), and the intensities can be written

$$I_\lambda = \tau_{\lambda_0} \times \left(\frac{\lambda}{\lambda_0} \right)^{-\beta} \times B_\lambda(T), \times N_H \quad (8)$$

where τ_{λ_0} is the optical depth at wavelength λ_0 , β is the spectral index, B_λ is the Planck function, and T the dust temperature. The SPIRE data alone do not allow the proper measurement of the dust temperature (the combination of SPIRE and PACS is mandatory, e.g., [Abergel et al., 2010]), so we decide not to include the dust temperature in our sky model and work in the Rayleigh-Jeans approximation, so that $B_\lambda(T) \propto \lambda^{-4}$. Moreover, we take $\beta = 2$, which is the "standard" value of the diffuse ISM (e.g., [Boulanger et al., 1996]). Finally, we have

$$\mathcal{X}(\alpha, \beta, \lambda) = \lambda^{-\varrho} \mathcal{X}(\alpha, \beta). \quad (9)$$

with $\varrho = 6$. However, as we will see in Section 2.2, the wavelength integration of the acquisition model will be done numerically. In other word, the spectrum profile is a degree of freedom that must be set in adequacy with the available knowledge about the observed sky.

Secondly, $\mathcal{X}(\alpha, \beta)$ is decomposed into a family of functions regularly shifted in space: $\psi_{ij}(\alpha, \beta) = \psi(\alpha - i\delta_\alpha, \beta - j\delta_\beta)$ where ψ is an elementary function and $(\delta_\alpha, \delta_\beta)$ are the shifts between the ψ_{ij} in (α, β) . We then have:

$$\mathcal{X}(\alpha, \beta) = \sum_{ij} x_{ij} \psi(\alpha - i\delta_\alpha, \beta - j\delta_\beta) \quad (10)$$

where ψ is the decomposition function and x are the coefficients.

One of the purposes of this decomposition is to describe the sky at a resolution possibly greater than the focal plane resolution. We therefore take an arbitrary nominal resolution corresponding to a target frequency width, greater than or equal to that of the data. To describe these maps, a natural approach is to choose ψ as the cardinal sine for which the frequency width is the target width (and a step δ equal to the inverse of this width) as described in Shannon's theory [Shannon & Weaver, 1948].

However, using cardinal sines requires analytical calculations that cannot be made explicit. To lighten the computational burden we will choose Gaussian ψ functions from now on. These functions are parametrized by their spatial shifts $(\delta_\alpha, \delta_\beta)$ and their standard deviations $(\sigma_\alpha, \sigma_\beta)$. The parameters $(\delta_\alpha, \delta_\beta)$ are chosen to be equal to the inverse of the target width as for the cardinal sines. In the numerical treatments of Section 4, the values of $(\delta_\alpha, \delta_\beta)$ are equal to the pointing increment of the *Large map* protocol, i.e. $2''$ [Orieux, 2009]. For the Gaussian function width parameters $(\sigma_\alpha, \sigma_\beta)$, we determined the value that minimizes the difference between the width at half-height of the cardinal sine and the Gaussian: $\sigma_{\alpha/\beta} \approx 0.6 \delta_{\alpha/\beta}$ in a similar manner in α and β .

2.2. Explicit calculation of acquisition model

Given the linearity of the instrument model (7) and the decomposition (9)-(10), the calculation of the model output for a fixed sky takes the form:

$$y_{lm}^n = \sum_{ij} x_{ij} \int \lambda^{-e} h_k(\lambda) \iiint \psi(\alpha - i\delta_\alpha - p_\alpha(t), \beta - j\delta_\beta - p_\beta(t)) h_o(\alpha - \alpha_{lm}, \beta - \beta_{lm}, \lambda) d\alpha d\beta h_b(nT_s - t) dt d\lambda. \quad (11)$$

Thus, to obtain the contribution of a sky coefficient x_{ij} to a data item y_{lm}^n , it is necessary to calculate four integrals, the discretization of which by brute force would result in very heavy numerical calculations.

Concerning the optics, the convolution of the function ψ with the optical response h_o appears in Eq. (11) and, as these are Gaussians, the convolution can be written

$$\begin{aligned} \iint \psi(\alpha - i\delta_\alpha - p_\alpha(t), \beta - j\delta_\beta - p_\beta(t)) h_o(\alpha - \alpha_{lm}, \beta - \beta_{lm}, \lambda) d\alpha d\beta \\ \propto \exp \left[-\frac{(p_\alpha(t) + i\delta_\alpha - \alpha_{lm})^2}{2\Sigma_\alpha^2} - \frac{(p_\beta(t) + j\delta_\beta - \beta_{lm})^2}{2\Sigma_\beta^2} \right] \end{aligned} \quad (12)$$

with, in a similar manner in α and β : $\Sigma_{\alpha/\beta}^2 = \sigma_{\alpha/\beta}^2 + \sigma_o^2$. This provides an explicit resolution of the spatial convolution.

For the integral over time, only the constant velocity phases can be explicitly described for the *Large map* protocol. In order to integrate over time in (11), we use the expressions of (2) for $p_\alpha(t)$ and $p_\beta(t)$, which gives

$$\begin{aligned} \sum_{ij} x_{ij} \int \lambda^{-e} h_k(\lambda) \int_t \exp \left[-\frac{(v_\alpha t + c_\alpha + i\delta_\alpha - \alpha_{lm})^2}{2\Sigma_\alpha^2} \right] \\ \exp \left[-\frac{(v_\beta t + c_\beta + j\delta_\beta - \beta_{lm})^2}{2\Sigma_\beta^2} \right] h_b(nT_s - t) dt d\lambda. \end{aligned} \quad (13)$$

It can be shown that explicit integration can be performed by including the Gaussians and the bolometer response (see details of the calculations in appendix B or in the supplements [Orieux, 2010]), and the model becomes

$$\begin{aligned} y_{lm}^n = \frac{S}{2\sqrt{2\pi}\Sigma_v} \sum_{ij} x_{ij} \int_\lambda \lambda^{-e} h_k(\lambda) \exp \left[-\frac{(o_\alpha + nT_s v_\alpha)^2}{2\Sigma_\alpha^2} - \frac{(o_\beta + nT_s v_\beta)^2}{2\Sigma_\beta^2} \right] \\ \operatorname{erfcx} \left(\frac{\Sigma_\alpha \Sigma_\beta}{\sqrt{2\tau}\Sigma_v} - \frac{\Sigma_\beta v_\alpha (o_\alpha + nT_s v_\alpha)}{\sqrt{2}\Sigma_\alpha \Sigma_v} - \frac{\Sigma_\alpha v_\beta (o_\beta + nT_s v_\beta)}{\sqrt{2}\Sigma_\beta \Sigma_v} \right) d\lambda. \end{aligned} \quad (14)$$

In this equation, the angles o_α and o_β are defined by: $o_\alpha = c_\alpha + i\delta_\alpha - \alpha_{lm}$ and $o_\beta = c_\beta + j\delta_\beta - \beta_{lm}$. Moreover, $\Sigma_v^2 = \Sigma_\beta^2 v_\alpha^2 + \Sigma_\alpha^2 v_\beta^2$.

The data point y_{lm}^n does not depend directly on the “scanning time” t as it is integrated and depends on time only through the sampling instants. These instants occur *only* in the form $o_\alpha + nT_s v_\alpha$ and $o_\beta + nT_s v_\beta$, and the equivalent spatial sampling is thus finer than the equivalent angular separation of the horns. The introduction of this spatial over-sampling produces spatial redundancy, which, properly modelled and taken into account, is a key element for reconstruction that is over-resolved relative to the focal plane resolution.

In addition, the time constant of the bolometer and the electronics τ appears only in the term $\Sigma_\alpha \Sigma_\beta / (\sqrt{2\tau}\Sigma_v)$, as an argument of the function erfcx . It is thus through this function erfcx that the influence of the bolometer and the electronics on the global *spatial* response of the system is taken into account.

The dependence on the wavelength through $\sigma_o(\lambda)$ makes explicit integration with respect to λ impossible. However, the integral depends neither on the data nor on the unknown object but only on the values defining the protocol. So, for a given protocol, these integrals can be calculated once and for all. Finally, the initial model brought in four integrations and the work described above makes three of them explicit.

Eq. (14) models the acquisition of the data item y_{lm}^n at time n by bolometer (l, m) from the coefficients x_{ij} that define the sky. These equations can be written

$$y_{lm}^n = \sum_{ij} x_{ij} \mathcal{H}_{lmn}(\psi_{ij}) \quad (15)$$

where \mathcal{H} is calculated from Eq. (14). The model is linear and we can thus write

$$\mathbf{y} = \mathbf{H}\mathbf{x} \quad (16)$$

where \mathbf{y} and \mathbf{x} are vectors of size LMN and IJ , and \mathbf{H} is a matrix of LMN rows and IJ columns, each row of which can be deduced from (14) by varying l, m, n for fixed i, j .

2.3. Invariant structure

Initially, the physical model (7) is based on convolutive (so invariant) transforms w.r.t. continuous variables. However, the discretization operation is irregular so the invariance property does not hold anymore. Nevertheless, the trace of this initial invariance continues to exist through the fact that \mathbf{H} is a *sum* of terms at different spatial positions of the Gaussians (cf. Eq. (14)). As the problem is now discretized, we seek to bring out an invariance by *quantified* shifts in

$$c_\alpha + i\delta_\alpha + nT_s v_\alpha - \alpha_{lm}$$

for the α direction, and similarly for β .

Consequently, the bolometers are positioned on a hexagonal grid that can be decomposed into two rectangular sub-grids of step P_α and P_β according to indices l and m . We thus have $\alpha_{lm} = lP_\alpha + mP_\beta$ and the position of the bolometers during scanning becomes

$$o_\alpha + nT_s v_\alpha = c_\alpha + i\delta_\alpha + nT_s v_\alpha - lP_\alpha - mP_\beta.$$

If all the terms are multiples of a common factor Δ_α , the continuous shift is

$$o_\alpha + nT_s v_\alpha = (n_0 + in_1 + nn_2 - ln_3 - mn_4)\Delta_\alpha.$$

This comes down to rounding the shifts to a multiple of Δ_α . It can be said that the actual position of the bolometers is shifted or that the data are interpolated to the nearest neighbour. The MADmap and SANEPIC methods use this idea but there is a notable difference: they perform the operation on a low-resolution grid, which results in limitation of the map resolution. In contrast, the developments proposed here exploit the idea of a high-resolution grid, enabling over-resolution or super-resolution reconstruction. By acting in the same way in the β direction, we have

$$y_{lm}^n = \sum_{ij} x_{ij} \mathcal{H}\left((n_0 + in_1 + nn_2 - ln_3 - mn_4)\Delta_\alpha, (n'_0 + in'_1 + nn'_2 - ln_3 - mn_4)\Delta_\beta\right)$$

and by computing the discrete convolution, we obtain

$$\tilde{y}(i', j') = \sum_{ij} x_{ij} \mathcal{H}\left((i - i')\Delta_\alpha, (j - j')\Delta_\beta\right). \quad (17)$$

Thus $y_{lm}^n = \tilde{y}(i', j')$ if and only if

$$i - i' = in_1 + ln_3 + mn_4 - nn_2 - n_0 \quad (18)$$

$$j - j' = jn'_1 + ln_3 + mn_4 - nn'_2 - n'_0. \quad (19)$$

In these conditions, the data \mathbf{y} , for a given scanning direction, are computed by discrete convolution (17) followed by (irregular) down-sampling defined by (18)-(19).

This structure allows the model output to be computed much more efficiently. First of all, the decomposition by convolution then decimation is faster than the direct calculation and, what is more, the convolution can be calculated by FFT. Finally, given that only the impulse response is necessary, there is no need to calculate and store all the elements of the matrix.

In this form, some calculations may be made even though they are useless, as the convolution is performed for all the indices whereas only some of them are used. The ratio depends on how fine the grid for the sky is relative to the size of the bolometer grid and the spatial shift. In practice, the excess calculation is reduced as we choose shifts $(\delta_\alpha, \delta_\beta)$ close to the delay between two sampling instants. Almost all the convolution results are observed.

There is, however, the disadvantage that the bolometer positions are approximated. Yet these positions are important because they allow to get the best out of the data and to properly manage the information needed to estimate high frequencies. We choose a step Δ that is close to the minimum shift of the bolometers, $P_\alpha/15$ at most for the smallest detector sampling step, i.e. about $\Delta \approx 2''$. The error introduced is thus small. This can be seen to be all the more valid when we consider the expected level of noise and telescope pointing errors, which are of the same order of magnitude, $2''$.

Finally, the initial model (16) is decomposed in the discrete convolution defined by (17) followed the (irregular) down-sampling defined by (18)-(19), that is to say \mathbf{H} is factorized and:

$$\mathbf{y} = \mathbf{H}\mathbf{x} = \mathbf{P}\mathbf{H}_c\mathbf{x} \quad (20)$$

where \mathbf{H}_c is a convolution matrix and \mathbf{P} a binary matrix that takes the values observed after the convolution. This is the pointing matrix similar to the one of SANEPIC and MADmap methods (but at a different resolution level). It has one, and only one, “1” per row since each data item can only come from one position. Some columns may be entirely zero as certain coefficients may not be observed. Conversely, some columns may contain several “1” because certain coefficients may be observed several times. From this, we also deduce that the matrix \mathbf{P} is a sparse matrix.

To sum up, by using an approximation on the position of the bolometers, we have separated the model \mathbf{H} , which has no particular structure, into two sub-models $\mathbf{H} = \mathbf{P}\mathbf{H}_c$ where \mathbf{H}_c is invariant and \mathbf{P} contains the non-invariant structure, which amounts to an irregular down-sampling. This decomposition is broadly similar to the one generally found in over-resolution in the field of image processing (see references in the Introduction).

Fig. 1 presents this decomposition for the PSW detector with a velocity of $30''/\text{s}$ towards the right: spatial redundancy contained in \mathbf{P} (the blacker the pixel, the more it has been observed) and spatial impulse response (the time response of the bolometer and the electronics is clearly visible as the spatial extent of the Gaussian lobe).

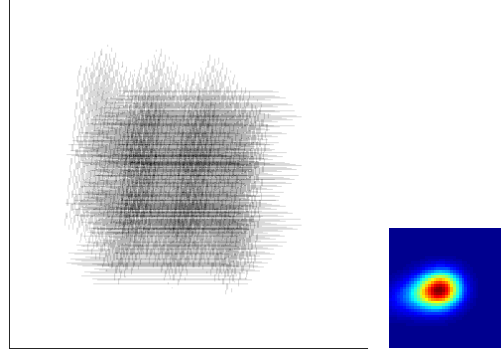


Figure 1. Factorized physical model (PSW detector, velocity of 30''/s towards the left): map of spatial redundancies P (left) and spatial impulse response H_c (right). The spatial scale are not proportional for better visualisation of the impulse response.

2.4. Conclusion

In conclusion, we have constructed a linear instrument model from the physical description of the phenomena involved during acquisition: scanning, optics, filters, bolometers and electronics are taken into account, together with a description of the sky in continuous variables in the three dimensions. We next explicitly described certain calculations and approached the model in a factorized form to lighten the numerical computation burden.

The model presented here differs from those currently used in SANEPIC [Patanchon et al., 2008] or MADmap [Cantalupo et al., 2010] in that it takes the physics of acquisition into consideration. Moreover, unlike monochromatic models [Sibthorpe et al., 2009], the sky model extends spectrally over the whole channel. Again unlike [Sibthorpe et al., 2009], our bolometer model is linearized, which simplifies the developments and allows the bolometer time response to be made clearly explicit.

Finally, the clear, consistent, global definition of the acquisition allows the spatial redundancy to be exploited directly and a processing method to be designed that uses these properties to estimate the sky at higher resolution than the focal plane resolution.

3. Data inversion for high resolution maps

The previous Section was dedicated to the instrument model describing the relationship between the measured data y and the unknown sky \mathcal{X} or its coefficients x through the equation

$$y = \mathcal{H}\mathcal{X} + n = Hx + n.$$

The matrix H is relatively complex and high-dimensional but the model (16) remains linear. The term n accounts for measurement and modelling errors and quantifies the data uncertainties. In this work, we consider that each bolometer denoted b is affected by an unknown offset o_b . Eq. (16) can be rewritten for the bolometer b

$$y_b = H_b x + o_b + n_b. \quad (21)$$

where y_b are data of bolometer b , H_b is the corresponding part of the instrument model and n_b accounts for errors at bolometer b . This Section presents the approach and methodology used to estimate the unknown x and the offsets o from the data y .

The question of sky reconstruction is a typical inverse problem and abundant literature is available on the subject [Idier, 2008; Demoment, 1989; Tikhonov & Arsenin, 1977; Twomey, 1962]. As presented in the previous Section, the instrument model embeds convolutions and low-pass systems. Consequently, data are poor for reliable image reconstruction. The inverse problem is ill-posed and this is particularly true when over-resolution is intended. In this context, a naive inversion, such as a least squares solution, would lead to an unacceptably noisy and unstable solution.

A usual class of solutions relies on regularization, i.e. the introduction of information [Idier, 2008; Demoment, 1989; Tikhonov & Arsenin, 1977; Twomey, 1962] to compensate for the lack of information in the data. A consequence of regularization is that reconstruction methods are specific to a class of map, according to the introduced information. From this standpoint, the present paper considers extended sources and relatively smooth maps. A secondary consequence of ill-posedness and regularization is the need to balance the compromise between different sources of information.

A possible solution relies on the TSVD [Hansen et al., 2000] that truncates the low singular values of \mathbf{H} that are practically responsible for noise amplification. Another approach [Richardson, 1972] stops the iterative algorithm before the solution is reached in order to prevent the occurrence of artefacts. The main drawbacks of these approaches are the unknown nature of the introduced information and the poor control (through a threshold or stopping criterion) of the trade-off with the data information.

As already pointed out, a relatively spatially regular sky is expected. Since it is defined as a function of continuous variables, the regularity can be measured by the energy of derivatives of the function \mathcal{X} . In the case of first derivatives in both directions, it can be shown (see appendix A) that

$$\left\| \frac{\partial \mathcal{X}(\alpha, \beta)}{\partial \alpha} \right\|^2 + \left\| \frac{\partial \mathcal{X}(\alpha, \beta)}{\partial \beta} \right\|^2 = \mathbf{x}^t (\mathbf{D}_\alpha + \mathbf{D}_\beta) \mathbf{x} \quad (22)$$

where $\mathbf{D} = \mathbf{D}_\alpha + \mathbf{D}_\beta$ is obtained from the autocorrelation of the basis ψ and is similar to a discrete gradient operator. This relation illustrates the equivalence between the measure on the continuous function \mathcal{X} and the measure on coefficient \mathbf{x} , thanks to the use of Gaussian decomposition²

With the regularity measure (22) and the white Gaussian hypothesis for \mathbf{n} , the solution is defined as the minimizer of the regularized least square criterion

$$\hat{\mathcal{X}}, \hat{\mathbf{o}} = \arg \min_{\mathcal{X}, \mathbf{o}} J_{\mathcal{X}}(\mathcal{X}, \mathbf{o}) \quad (23)$$

where

$$J_{\mathcal{X}}(\mathcal{X}, \mathbf{o}) = \|\mathbf{y} - \mathcal{H}\mathcal{X} - \mathbf{o}\|^2 + \mu \left(\left\| \frac{\partial \mathcal{X}(\alpha, \beta)}{\partial \alpha} \right\|^2 + \left\| \frac{\partial \mathcal{X}(\alpha, \beta)}{\partial \beta} \right\|^2 \right). \quad (24)$$

The parameter μ tunes the trade-off between adequation to the data and smoothness of the map. Since the set of ψ_{ij} forms the basis of the function space, \mathcal{X} can be expressed with a unique set $\hat{\mathbf{x}}$

$$\hat{\mathcal{X}}(\alpha, \beta) = \sum_{ij} \hat{x}_{ij} \psi(\alpha - i\delta_\alpha, \beta - j\delta_\beta).$$

² As an alternative, a non-quadratic norm of the derivative, e.g. convex penalties, could also be used. The interest of this is less penalization of high gradients in the map. Unfortunately, an explicit measure on coefficients, as in the quadratic norm, is not explicit.

The criterion Eq. (24) is defined on \mathcal{X} but the same solution is obtained with an equivalent criterion on the coefficient

$$\hat{\mathbf{x}}, \hat{\mathbf{o}} = \arg \min_{\mathbf{x}, \mathbf{o}} J_{\mathbf{x}}(\mathbf{x}, \mathbf{o})$$

where

$$J_{\mathbf{x}}(\mathbf{x}, \mathbf{o}) = \|\mathbf{y} - \mathbf{H}\mathbf{x} - \mathbf{o}\|^2 + \mu \mathbf{x}^t \mathbf{D} \mathbf{x} \quad (25)$$

and the property

$$J_{\mathbf{x}}(\hat{\mathbf{x}}, \hat{\mathbf{o}}) = J_{\mathcal{X}}(\hat{\mathcal{X}}, \hat{\mathbf{o}}). \quad (26)$$

Remark 1. – A Bayesian interpretation of criterion (25) is the Gaussian *posterior* law

$$p(\mathbf{x}, \mathbf{o} | \mathbf{y}) \propto p(\mathbf{y} | \mathbf{x}, \mathbf{o}) p(\mathbf{x}) p(\mathbf{o}) \\ \propto \exp \left[-\frac{1}{2\sigma_n^2} \|\mathbf{y} - \mathbf{H}\mathbf{x} - \mathbf{o}\|^2 - \frac{1}{2\sigma_x^2} \mathbf{x}^t \mathbf{D} \mathbf{x} \right].$$

with Gaussian iid likelihood, Gaussian correlated prior and flat prior law on \mathbb{R} for \mathbf{o} . Consequently, the minimum of the criterion is the maximum of this law

$$\hat{\mathbf{x}}, \hat{\mathbf{o}} = \arg \max_{\mathbf{x}, \mathbf{o}} p(\mathbf{x}, \mathbf{o} | \mathbf{y})$$

where $\mu = \sigma_x^2 / \sigma_n^2$. An advantage of the Bayesian interpretation is the ability to derive an uncertainty around the maximum through the variance (see Sec. 4) of the *posterior* law. Another important advantage of the Bayesian interpretation deals with the estimation of μ and of instrument parameters and we have a second paper devoted to this point [Orieux et al., 2010].

The proposed algorithm for the computation of $\hat{\mathbf{x}}$ and $\hat{\mathbf{o}}$ is an alternate minimization algorithm: after an initialization, the following two steps are repeated

1. Find $\hat{\mathbf{x}}$ for fixed \mathbf{o}

$$\hat{\mathbf{x}}^k = \arg \min_{\mathbf{x}} \|\mathbf{y} - \mathbf{H}\mathbf{x} - \hat{\mathbf{o}}^k\|^2 + \mu \mathbf{x}^t \mathbf{D} \mathbf{x} \quad (27)$$

2. Find $\hat{\mathbf{o}}$ for fixed \mathbf{x}

$$\hat{\mathbf{o}}^{k+1} = \arg \min_{\mathbf{o}} \|\mathbf{y} - \mathbf{H}\hat{\mathbf{x}}^k - \mathbf{o}\|^2 \quad (28)$$

until a criterion is met. For fixed \mathbf{x} , the solution is straightforward and $\hat{\mathbf{o}}_b$ is the empirical mean of the residual $\mathbf{y}_b - \mathbf{H}_b \mathbf{x}$ for each bolometer separately. For fixed \mathbf{o} , the solution Eq. (27) is unique (because the criterion is convex) and explicit

$$\hat{\mathbf{x}} = (\mathbf{H}^t \mathbf{H} + \mu \mathbf{D})^{-1} \mathbf{H}^t (\mathbf{y} - \mathbf{o}). \quad (29)$$

The estimator is linear w.r.t. data \mathbf{y} . Unfortunately, since \mathbf{H} is not circulant, $\hat{\mathbf{x}}$ cannot be computed with a “brute force” algorithm: the practical inversion of the Hessian matrix $\mathbf{H}^t \mathbf{H} + \mu \mathbf{D}$ is impossible (the size of this matrix is the square of the number of coefficients \mathbf{x}). The proposed solution relies on an iterative conjugated gradient descent algorithm [Nocedal & Wright, 2000; Shewchuk, 1994]. Because of the convexity and differentiability of the criterion, the algorithm is guaranteed to converge to the solution.

The conjugated gradient is a first order algorithm that operates the gradient \mathbf{g}_k at current point \mathbf{x}_k

$$\mathbf{g}_k = 2\mathbf{H}^t(\mathbf{y} - \mathbf{o}) - 2(\mathbf{H}^t\mathbf{H} + \mu\mathbf{D})\mathbf{x}_k \quad (30)$$

to compute a new point. As illustrated by Eq. (30), the most expensive part is the computation of the product between the matrix $\mathbf{H}^t\mathbf{H}$ and the current point \mathbf{x}_k .

Remark 2. – As described in appendix A, the regularization part $\mathbf{D}\mathbf{x}_k$ is computed by FFT. Moreover, as described in appendix C the model-related part $\mathbf{H}^t\mathbf{H}\mathbf{x}_k$ can also be efficiently computed based on FFT, decimation and zero-padding.

4. Experimental results

This part illustrates the improvement that our approach can bring, first using simulated data and then with actual data transmitted by Herschel.

4.1. Simulated data

4.1.1. Experimental protocol

We chose three $20' \times 20'$ maps used by the SPIRE consortium to assess reconstruction methods [Clements et al., 2006]: (i) a map of galactic cirrus (Fig. 4) complying with the *a priori* regularity model, (ii) a map of galactic cirrus superimposed on point sources (Fig. 7) and (iii) a galaxy map (Fig. 8).

The study concerns the PMW channel and the *Large Map* protocol with three scans in each direction and a velocity of $30''/\text{s}$. The data were generated by the instrument model (16), considering for this simulation part that the bolometers are not affected by any offset. Moreover, the sky spectrum profile is a degree of freedom of our acquisition model since the wavelength integration is numerical (Eq. (14)). The profile have to be set in adequacy with available knowledge about the sky, see Section 2.1.5. We assume for the simulations and the inversions that the sky spectrum is flat ($\varrho = 0$). The noise is zero-mean white Gaussian noise and we consider three levels characterized by their standard deviation σ_n (“standard noise” hereafter), $10\sigma_n$ (“high noise”) and $0.1\sigma_n$ (“low noise”). The standard deviation is the same for all the bolometers and, unless stated otherwise, all the data sets were generated with the same noise realization.

The proposed reconstruction for the $20' \times 20'$ maps are performed using $\delta_\alpha = \delta_\beta = 2''$, i.e. maps of 600×600 coefficients. Our results are compared with the map obtained by coaddition, with $6''$ as pixel size.

In accordance with what was presented in Section 3, the map is reconstructed as the minimizer of criterion (23)-(25) and the minimization is performed by a conjugate gradient algorithm with optimal step size. Fig. 2 illustrates the behaviour of the algorithm for cirrus in the “standard noise” case. As expected, the value of the criterion decreases at each iteration and stabilizes. A few tens of iterations appear to be sufficient to reach the minimum in the example presented and in the other tested examples.

In the simulated cases, as the original map (the “sky truth”) is known, we can make a quantitative assessment of the reconstruction through an error measure defined by:

$$e = \sum_{i,j} |x_{ij}^* - \widehat{x}_{ij}| / \sum_{i,j} |x_{ij}^*| \quad (31)$$

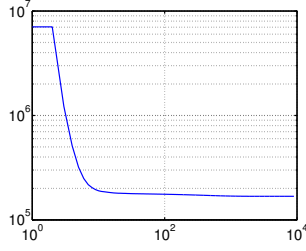


Figure 2. Value of the criterion during iterations of the minimization algorithm (conjugate gradient with optimal step). Case of cirrus with “standard noise”.

where \mathbf{x}^* is the true map and $\hat{\mathbf{x}}$ is the reconstructed map. These measures enable the errors produced by the different methods to be compared quantitatively.

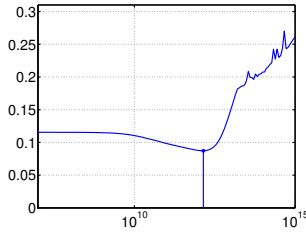


Figure 3. Reconstruction error e vs regularization parameter μ . Case of cirrus with “standard noise”.

In the case of the proposed reconstruction, the estimate depends on the regularization parameter: $\hat{\mathbf{x}} = \hat{\mathbf{x}}(\mu)$. Fig. 3 illustrates this dependence through the error e for cirrus in the “standard noise” case. A non-zero optimum value μ_{opt} appears (here $\sim 10^{12}$) for which e is a minimum, thus confirming the interest of the regularization. A value lower than 10^{11} leads to an under-regularized map and a value greater than 10^{13} to an over-regularized one. In the following, it is, of course, the optimal value that is used to reconstruct the maps. Also, as far as the map sensitivity to the regularization parameter is concerned, it appears empirically that μ needs to vary by a factor 2 around μ_{opt} for a visible modification of the map to be obtained. This result is confirmed in Fig. 3, where the minimum is not very marked relative to the horizontal scale. Fig. 3 also quantifies the improvement provided by the regularization: the errors for the non-regularized and optimal-regularized maps are 0.12 and 0.08 respectively, i.e. a gain of 33%.

4.1.2. Restoration of galactic cirrus

Fig. 4 sums up the first results concerning the cirrus in the “standard noise” case. The proposed map is very close to the true one. In particular, our method restores details of small spatial scales (with spectral extension from low to high frequency) that are invisible on the coaddition but present on the true map (see also the profiles in Figs. 4(d) and 4(e)). In particular, the fluctuations around pixels 250 and 350 are well restored. In addition, our method also correctly restores large-scale structures, corresponding to low-frequencies down to the null frequency (mean level of the map). We conclude that our method properly estimate the correct photometry.

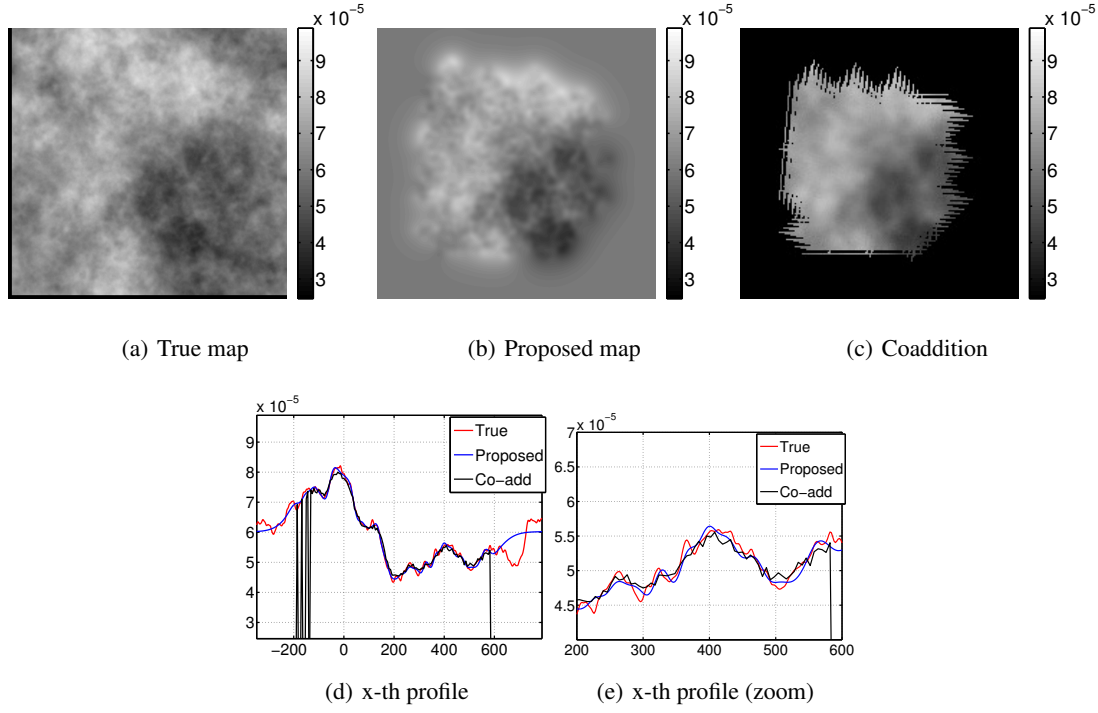


Figure 4. Comparison of results. Fig. 4(a) shows the true map, Fig. 4(b) presents the proposed map and Fig. 4(c) the coaddition. A horizontal profile is shown in Fig. 4(d) and Fig. 4(e) gives a zoom.

Remark 3. – Moreover, the reconstruction method is linear with respect to the data (see Section 2), which means that the use of arbitrary units is valid.

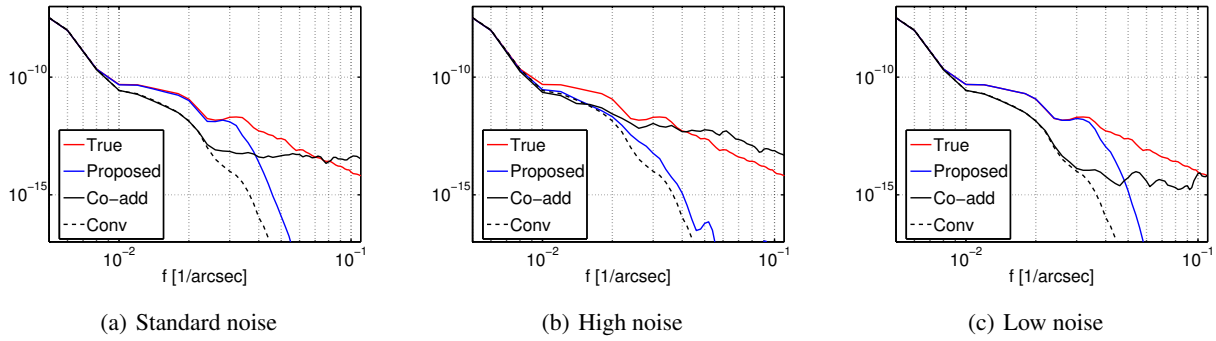


Figure 5. Circular means of power spectra for the three levels of noise (standard deviations: σ_n , $10 \sigma_n$ and $0.1 \sigma_n$).

To quantify the gain in correctly restored bandwidth, we look at the power spectra of the maps (Fig. 5) for the true sky, the sky convolved with the PSF, the coaddition and the proposed sky. As mentioned in Section 2.1.2, the sampling frequency of the focal plane is $f_s \approx 0.02 \text{ arcsecond}^{-1}$. Consequently, by the Shannon theorem, the acquired data during one integration cannot correctly represent frequencies above $f_s/2 \approx 0.01 \text{ arcsecond}^{-1}$. We have also seen in Section 2.1.2 that the FWHM of the PSF is $25.2''$ at $350 \mu\text{m}$, i.e. a cutoff frequency of the optical transfer function of $\approx 0.04 \text{ arcsecond}^{-1}$. The attenuation effect of the convolution by the PSF on the true map

(or of the multiplication of the Fourier transform by the transfer function) is visible on the power spectra of the convolved and coaddition maps, for all frequencies above $\approx 0.008 \text{ arcsecond}^{-1}$ (Fig. 5).

Regarding our approach, the power spectra of the proposed map perfectly follows the power spectra of the true map, from the null frequency up to a limit frequency that depends on the noise level. In the “standard noise” case, Fig. 5(a), this limit is $0.03 \text{ arcsecond}^{-1}$ that is to say three times the limit frequency of each integration ($f_s/2 \approx 0.01 \text{ arcsecond}^{-1}$). It illustrates that our method also takes full advantage of the high frequency temporal sampling. In any case and compared to the coaddition, we have multiplied by a factor ≈ 4 the spectral bandwidth (starting from the null frequency) where frequencies attenuated by the optical transfer function are accurately corrected. The high-resolution reconstruction potentiality of the proposed method is clearly demonstrated in this experiment.

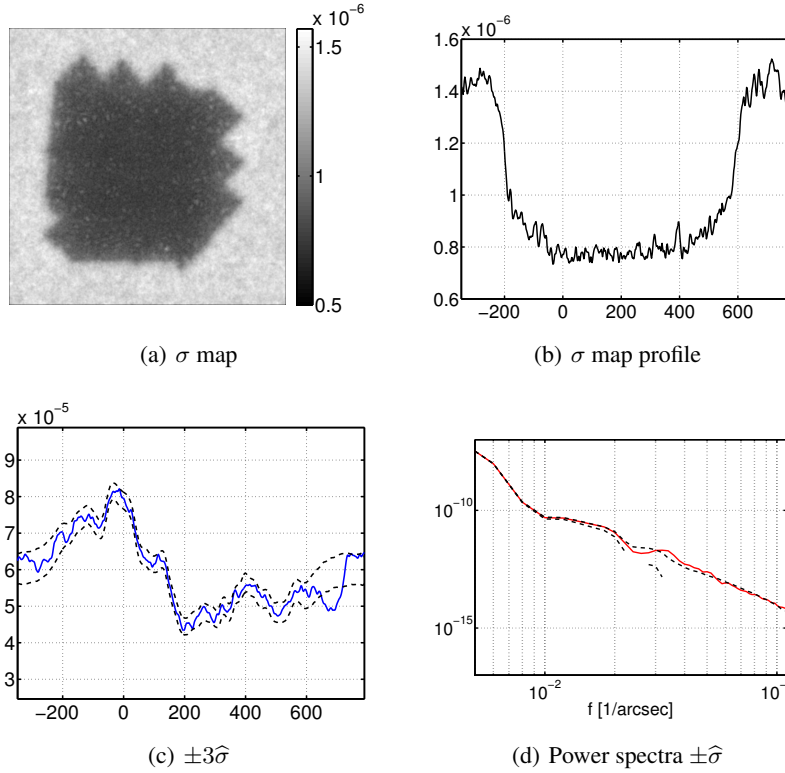


Figure 6. Uncertainty provided by the *a posteriori* standard deviation $\hat{\sigma}$. Fig. 6(a) shows the map of the standard deviation for each pixel and Fig. 6(b) gives a profile. Fig. 6(c) shows a profile of the *true map* as a solid line and the two dashed line give a $\pm 3\hat{\sigma}$ interval around the *estimated map*. Fig. 6(d) shows the PSD of the *true map* as a solid red line and the two dashed line give a $\pm \hat{\sigma}$ interval around the *estimated PSD map* in the “standard noise” case.

Our method also gives a value for the uncertainty on each pixel through the Bayesian interpretation presented in Remark 1. This uncertainty is provided by the standard deviation $\hat{\sigma}$ of the *a posteriori* law and a map of these standard deviations is shown in Fig. 6(a). The uncertainty is naturally smaller in the centre of the map and grows as we move away from the centre because the data contain less information. Fig. 6(b) shows a profile of the uncertainty and Fig. 6(c) gives a profile of the *true map* and a $\pm 3\hat{\sigma}$ interval around the *estimated map*. We thus

show that the true map is indeed inside the interval around the estimated one. The Fig. 6(d) gives the true PSD and a $\pm 1\hat{\sigma}$ interval the estimated PSD. Again, up to the 0.03 frequency limit, the true PSD is inside the interval.

The possibilities of restoring frequencies obviously depend on the noise levels. Fig. 5 compares the spectra obtained with the three noise levels, the parameter μ being chosen to be optimal each time from the point of view of the error Eq. (31). When the noise level is lower, it is possible to restore slightly higher frequencies: up to 0.03 arcsecond⁻¹ for “low noise”, as against 0.025 arcsecond⁻¹ for “standard noise”. Conversely, in the case of “high noise”, our method no longer restores the frequencies attenuated by the optical transfer function Fig. 5(b). The deconvolution effect is reduced and the essential effect is one of denoising. Nevertheless, the proposed method gives better (or equivalent) results than coaddition in all cases.

4.1.3. Other types of sky

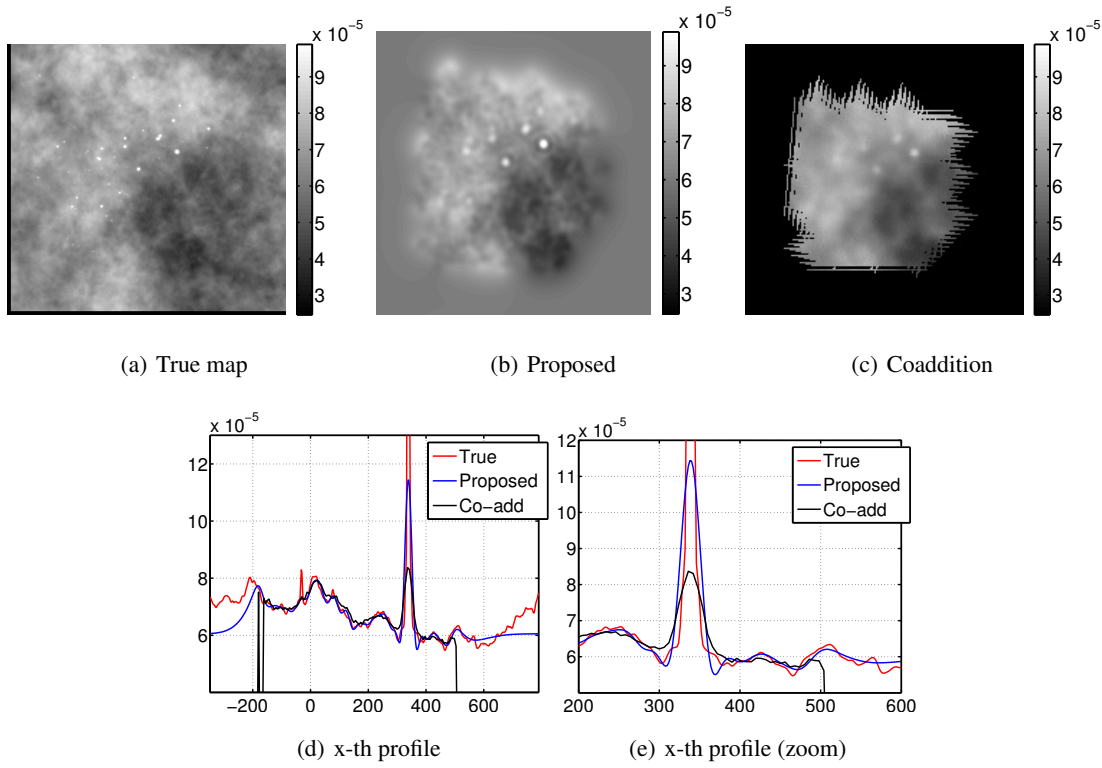


Figure 7. Restoration of cirrus superimposed on point sources.

Our method is based on spatial regularity information. To assess how robust it is, we tested it with two other types of sky in which the spatial regularity is less pronounced: galactic cirrus superimposed on point sources, and a galaxy image. The results obtained are presented in Figs. 7 and 8.

For the first case, the characteristics of the reconstructions can be seen on the maps by comparing Fig. 7(b) and Fig. 7(c): the coaddition map is smoother than the one we propose. In addition, some of the point sources of the true map are visible on the proposed map but not on the coaddition one. If we observe the profiles presented in Fig. 7(d), we note that the point source near pixel 350 is underestimated but markedly less so by the proposed method than

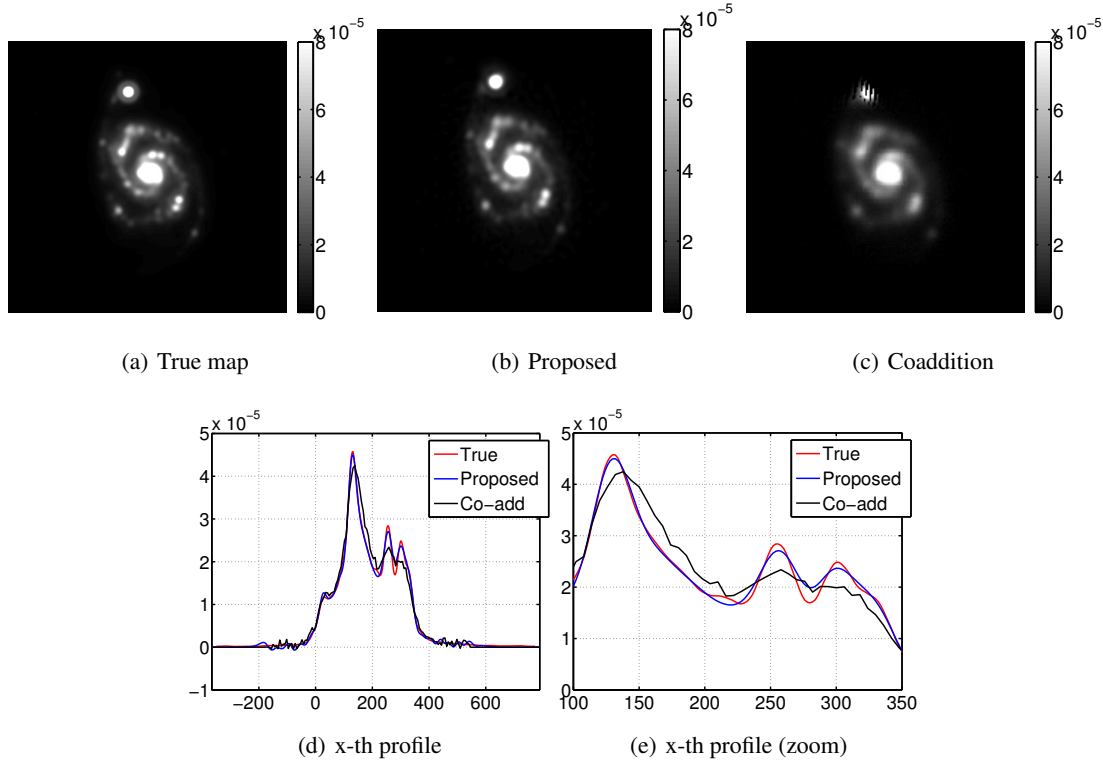


Figure 8. Restoration of galaxy.

by coaddition. Rebounds also appear around the point sources, a feature characteristic of linear deconvolution (resulting from a quadratic criterion) in the presence of point sources.

The galaxy does not contain point sources but has spatial structures that are more complex than the galactic cirrus. These structures are considerably better restored by our method than by coaddition and the comparison between Fig. 8(b) and Fig. 8(c) is instructive from this point of view. In particular, the double structures in the arms of the true galaxy (Fig. 8(a)) are correctly separated by the proposed method (Fig. 8(b)) but not by coaddition (Fig. 8(c)). Moreover, while the profile of Fig. 8(d) shows real restoration of the fluctuations between pixels 200 and 400 by both the proposed method and coaddition, the proposed restoration is clearly superior to coaddition.

In conclusion, the proposed method is relatively flexible and shows a good restoration capacity for various types of map. In particular, it possesses a certain robustness with respect to an input sky presenting characteristics that are poorly taken into account by the *a priori* model based on regularity information. It provides a sky that is closer to the real one than that obtained by coaddition, even in the least favourable cases.

4.2. Processing real data

We conducted the first tests with real data of the reflection nebula NGC 7023 and of the Polaris flare (which is a high Galactic latitude cirrus cloud) performed during the science demonstration phase of Herschel and already presented in [Abergel et al., 2010] and [Miville-Deschênes et al., 2010], respectively. In order to run our algorithm, we took the Level-1 files processed using HIPE. The true sky is not known, of course, so the value of the regularization parameter was fixed for each of the spectral channel by a trade-off between the gain in spectral resolution and the amplification of the $1/f$ noise.

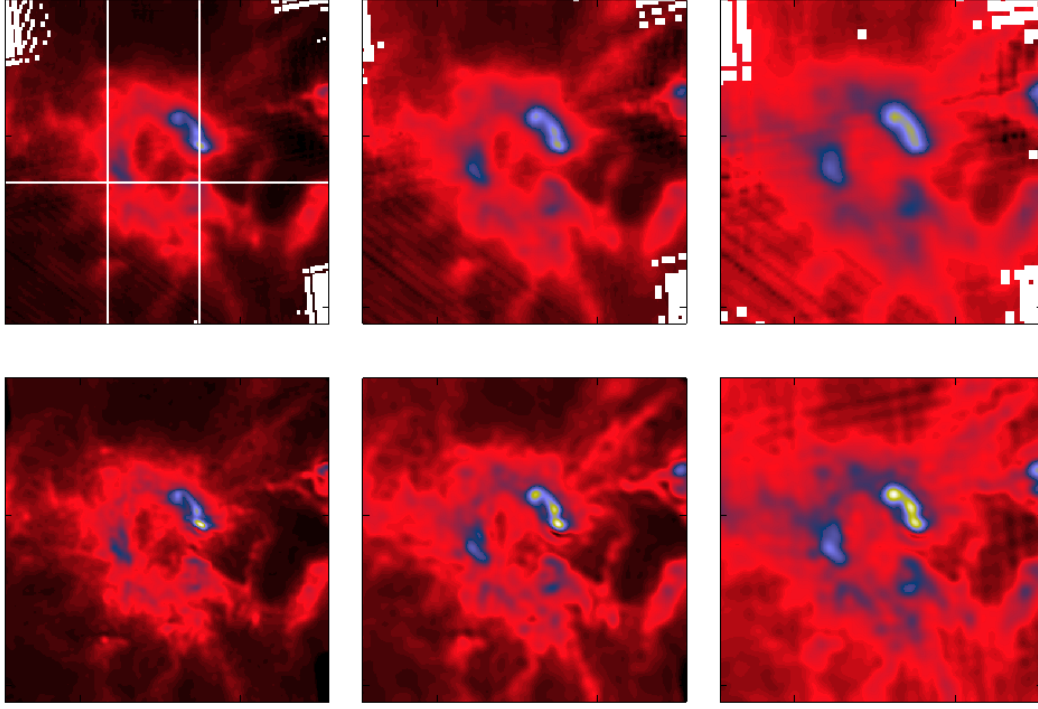


Figure 9. Central part ($23' \times 23'$) of NGC 7023 in the three channels. Top panels: coadded maps; bottom panels: proposed map.

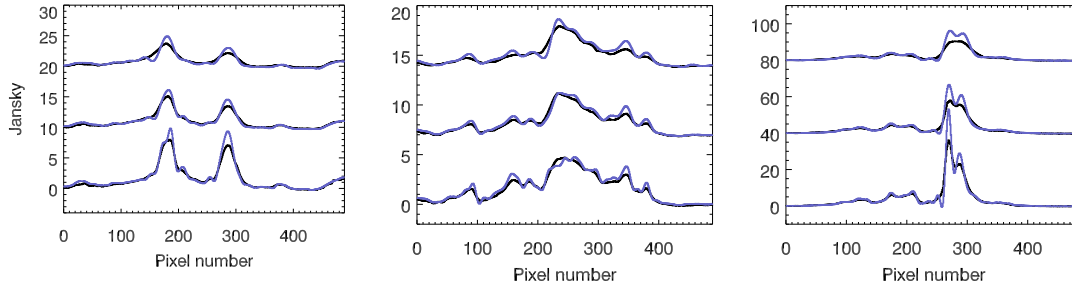


Figure 10. Brightness profiles along the three sections shown in the top left panel of Fig. 9. Each panel shows the profiles along one section within the PSW, PMW and PLW channel, offset for clarity from bottom to top respectively. Left panel: horizontal profile; central and right panels: vertical profiles. Coefficient are $2''$ spaced. Black: coadded maps, blue: proposed maps.

Figs. 9 to 12 illustrate the results for NGC 7023 and the polaris flare. The gain in spatial resolution is spectacular in the three channels. It is interesting to note that the map of NGC 7023 obtained by our method in the longest wavelength channel ($500 \mu\text{m}$, the PLW channel) shows spatial structures that are not visible in the coaddition but are real since they are visible at shorter wavelengths, as illustrated for instance on the last panel of Fig. 10. The same panel also shows that negative rebounds appear on the sharpest side of the brightest filament of NGC 7023. This filament is the narrowest structure of the map and its width is comparable to the width of a point source. Comparable rebounds were also seen on our simulations with point sources (Fig. 7). The Polaris flare does not contain comparable bright and narrow filament, so the proposed map does not present this kind of artifact.

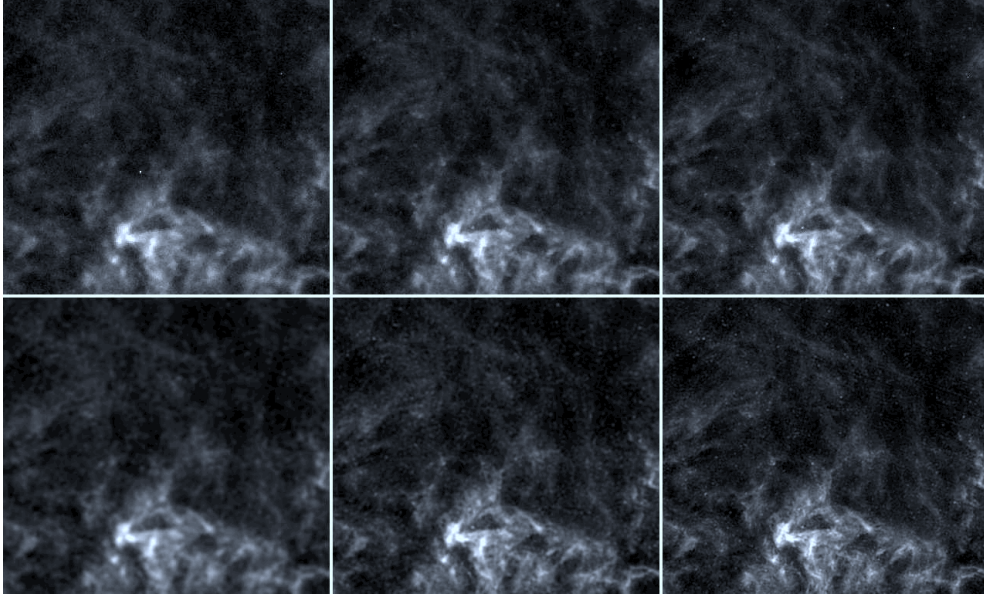


Figure 11. $50' \times 50'$ square in the Polaris flare (the total field observed during the science demonstration phase of Herschel is presented in [Miville-Deschênes et al., 2010]). Top panels and from left to right: coadded maps in the PLW, PMW and PSW channels, respectively; bottom panels: proposed results in the three channels.

Fig. 12 shows that the power spectrum of the proposed map of the Polaris flare in the PSW channel follows the expected power law typical of the infrared emission of high Galactic cirrus $P(k) \propto k^\gamma$ with $\gamma = -2.7$ (e.g., [Miville-Deschênes et al., 2010]) on a frequency range from $10^{-3} \text{ arcsecond}^{-1}$ to $3 \times 10^{-2} \text{ arcsecond}^{-1}$. As for simulated data, Section 4.1, the attenuation by the Optical Transfer Function (OTF) is accurately corrected up to the frequency where the noise is dominant. Thanks to this correction, the contrast of the small scale structures in the maps is enhanced (Figs. 11 and 12), since the energy of each structure is put in a smaller number of pixels than for the co-added case.

5. Conclusion

We have proposed a new generic method of over-resolved (with respect to the detector resolution) reconstruction of images for scanning instruments and have applied it to the SPIRE instrument of the Herschel observatory.

The first key element is an instrument model that precisely describes the physical processes involved in the acquisition. To explain the data in a reliable way, our model combines the descriptions of three elements: (i) the sky as a function of continuous variables in the three dimensions (two spatial and one spectral), (ii) the optics and the rest of the instrumentation (bolometer, electronics,...) and (iii) the scanning strategy. We thus arrive at a linear model in integral form (Eq. (7)). We then write this as a matrix expression (Eq. (16)) by making certain calculations explicit. Next, by coming close to the pointed positions (on a high-resolution grid), we decompose it into a convolution followed by (irregular) down-sampling (Eq. (20)). This model provides the most faithful link between the data, the sky actually observed, and the instrument effects.

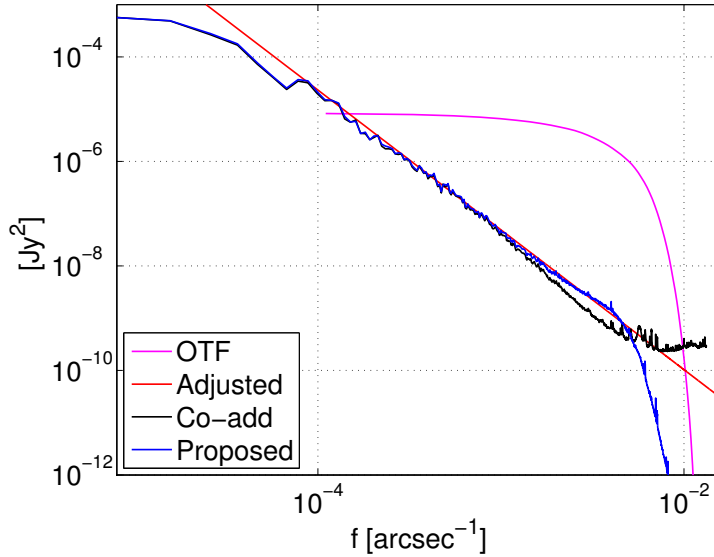


Figure 12. Circular means of the power spectrum of the $50' \times 50'$ square shown on Fig.11 and in the PSW channel. The red line shows the power law $P(k) \propto k^\gamma$ adjusted on the data in a frequency range from $10^{-3} \text{ arcsecond}^{-1}$ to $3 \times 10^{-2} \text{ arcsecond}^{-1}$, with $\gamma = -2.7$. At smaller frequencies, [Miville-Deschênes et al., 2010] have shown that the SPIRE spectra are attenuated compared to IRAS, which is likely due to the correction of $1/f$ noise attributed to thermal drifts in the preprocessing of the data. The pink solid line shows the Optical Transfer Function (OTF).

On the sole basis of this instrument model and the data, the inversion is an ill-posed problem. The lack of information brought by the data, considering the limitations of the instrument, leads to instability of the inversion, which is all the more noticeable when the target resolution is high. This difficulty is overcome by a standard regularization method that constitutes the second key element. The method relies on spatial regularity information introduced by quadratic penalization and on a quadratic data attachment term, the trade-off being governed by a regularization parameter. Thus, the inversion is based on a relatively standard linear approach and its implementation uses standard numerical optimization tools (conjugate gradient with optimal step).

The presented results for the SPIRE instrument give a spectacular illustration, on simulated and real data, of the potential of our method. Through the use of the accurate instrument model and *a priori* regularity information, we restore spatial frequencies over a bandwidth ~ 4 times that obtained with coaddition. In all channels, the attenuation by the optical transfer function is accurately corrected up to the frequency where the noise is dominant. The photometry is also properly restored.

There are two main straightforward perspectives to our method: firstly, the instrument parameters must be known and, secondly, the regularization parameter must be arbitrarily chosen. Future work will propose a “non-supervised” and “myopic” inversion method for setting these parameters automatically.

As other perspective, quadratic prior adequacy is known for possible excessive sharp edges penalization in the restored object. The use of convex $L_2 - L_1$ penalization [Künsch, 1994; Charbonnier et al., 1997] can overcome this limitation. Secondly, estimation of parameters of correlation matrix (cutoff frequency, attenuation coefficients, spectral profile, ...) could be achieved for the correlation matrix of the object or the noise (typically for the $1/f$ noise).

Finally, a really valuable perspective could be to introduce the spectral dependence between the different channels in the data inversion. The conjunction with a PACS direct model and the joint inversion of SPIRE and PACS data would greatly improve the map reconstruction.

Acknowledgment

The authors would like to thank M. Griffin (CSPA – Cardiff University), B. Sibthorpe (UKATC – Royal Observatory Edinburgh) and G. Le Besnerais (DTIM – ONERA), for fruitful discussions and CNES for supporting.

Appendix A: Energy spectral density

This appendix gives the details of the calculations concerning the regularity measure and its frequency interpretation, which are used in Section 3. Based on the decomposition of Eq. (10), the energy of the first derivative can be written

$$\begin{aligned} \left\| \frac{\partial \mathcal{X}}{\partial \alpha} \right\|^2 &= \iint_{\mathbb{R}^2} \left(\frac{\partial \mathcal{X}}{\partial \alpha} \right)^2 d\alpha d\beta \\ &= \sum_{ij i' j'} x_{ij} x_{i' j'} \iint_{\mathbb{R}^2} \left(\frac{\partial}{\partial \alpha} \psi_{i' j'} \right) \left(\frac{\partial}{\partial \alpha} \psi_{ij} \right) d\alpha d\beta \end{aligned}$$

By noting the derivative $\psi'_\alpha = \partial \psi / \partial \alpha$, we bring out the autocorrelation $\Psi_\alpha = \psi'_\alpha \star \psi'_\alpha$ of the first derivative of the decomposition function and we have

$$\begin{aligned} \left\| \frac{\partial \mathcal{X}}{\partial \alpha} \right\|^2 &= \sum_{ij i' j'} x_{ij} x_{i' j'} \iint_{\mathbb{R}^2} \psi'_\alpha(\alpha - i' \delta_\alpha, \beta - j' \delta_\beta) \psi'_\alpha(\alpha - i \delta_\alpha, \beta - j \delta_\beta) d\alpha d\beta \\ &= \sum_{ij i' j'} x_{ij} x_{i' j'} [\psi'_\alpha \star \psi'_\alpha] \{(i' - i) \delta_\alpha, (j' - j) \delta_\beta\} \\ &= \sum_{ij i' j'} x_{ij} x_{i' j'} \Psi_\alpha \{(i' - i) \delta_\alpha, (j' - j) \delta_\beta\} \end{aligned} \quad (\text{A.1})$$

As there is a finite number of coefficients x_{ij} , the measure can be put in the form of a quadratic norm

$$\left\| \frac{\partial \mathcal{X}}{\partial \alpha} \right\|^2 = \mathbf{x}^t \mathbf{D}_\alpha \mathbf{x}$$

where the matrix \mathbf{D}_α is obtained from Ψ_α . Considering the invariant structure of (A.1), the matrix \mathbf{D}_α has a Töeplitz structure. The calculation is performed by discrete convolution and can be done by FFT.

By introducing the dimension β :

$$\left\| \frac{\partial \mathcal{X}}{\partial \alpha} \right\|^2 + \left\| \frac{\partial \mathcal{X}}{\partial \beta} \right\|^2 = \mathbf{x}^t \mathbf{D}_\alpha \mathbf{x} + \mathbf{x}^t \mathbf{D}_\beta \mathbf{x}$$

The quadratic regularity measure on the function \mathcal{X} with continuous variables is expressed through a quadratic regularity measure on the coefficients \mathbf{x} .

The autocorrelation Fourier transform (FT) is the energy spectral density, i.e. the squared modulus of the FT of ψ'_α

$$\begin{aligned} \mathring{\Psi}_\alpha(f_\alpha, f_\beta) &= \iint_{\mathbb{R}^2} \Psi_\alpha(\alpha, \beta) e^{-2j\pi(\alpha f_\alpha + \beta f_\beta)} d\alpha d\beta \\ &= \left| \iint_{\mathbb{R}^2} \psi'_\alpha(\alpha, \beta) e^{-2j\pi(\alpha f_\alpha + \beta f_\beta)} d\alpha d\beta \right|^2 \\ &= 4\pi^2 f_\alpha^2 \left| \psi(f_\alpha, f_\beta) \right|^2 \end{aligned}$$

where $\overset{\circ}{\psi}$ is the FT of ψ . When the dimension β is introduced, the *a priori* energy spectral density for the sky naturally has circular symmetry

$$\overset{\circ}{\Psi}(f_\alpha, f_\beta) = 4\pi^2 (f_\alpha^2 + f_\beta^2) \left| \overset{\circ}{\psi}(f_\alpha, f_\beta) \right|^2. \quad (\text{A.2})$$

This calculation brings out the frequency structure introduced *a priori* for the sky according to the chosen function ψ . This is a high-pass structure since the factor $f_\alpha^2 + f_\beta^2$ tends to cancel $\overset{\circ}{\Psi}$ around zero, which is consistent with a regularity measure.

Appendix B: Explicit calculation of the model

In order to integrate over time in (13), we use the expressions of (2) for $p_\alpha(t)$ and $p_\beta(t)$, which give

$$\frac{1}{2\pi} \frac{1}{\Sigma_\alpha \Sigma_\beta} \int_t \exp \left[-\frac{1}{2} \frac{(v_\alpha t + c_\alpha + \alpha^{ij} - \alpha_{lm})^2}{\Sigma_\alpha^2} \right] \exp \left[-\frac{1}{2} \frac{(v_\beta t + c_\beta + \beta^{ij} - \beta_{lm})^2}{\Sigma_\beta^2} \right] h_b(nT_s - t) dt.$$

With the bolometer response

$$h_b(nT_s - t) = \mathbb{1}_{[0 + \infty[}(nT_s - t) S \exp \left[-\frac{nT_s - t}{\tau} \right],$$

we have

$$\frac{1}{2\pi} \frac{S}{\Sigma_\alpha \Sigma_\beta} \exp \left[-\frac{nT_s}{\tau} \right] \int_{-\infty}^{nT_s} \exp \left[-\frac{1}{2} \frac{(v_\alpha t + o_\alpha)^2}{\Sigma_\alpha^2} \right] \exp \left[-\frac{1}{2} \frac{(v_\beta t + o_\beta)^2}{\Sigma_\beta^2} \right] \exp \left[\frac{t}{\tau} \right] dt \quad (\text{B.1})$$

with $o_\alpha = c_\alpha + \alpha^{ij} - \alpha_{lm}$ and $o_\beta = c_\beta + \beta^{ij} - \beta_{lm}$. This is the integration of a truncated Gaussian as the argument of the exponential has a form that is quadratic in t .

B.1. Calculation of the argument

Here, we express the quadratic form in question

$$-\frac{1}{2} \frac{\tau \Sigma_\beta^2 (v_\alpha t + o_\alpha)^2 + \tau \Sigma_\alpha^2 (v_\beta t + o_\beta)^2 - 2 \Sigma_\alpha^2 \Sigma_\beta^2 t}{\Sigma_\alpha^2 \Sigma_\beta^2 \tau} = -\frac{1}{2} \frac{n(t)}{\Sigma_\alpha^2 \Sigma_\beta^2 \tau}.$$

Developing and factorizing the numerator $n(t)$ gives it the form

$$\begin{aligned} n(t) &= \tau \Sigma_\beta^2 (v_\alpha^2 t^2 + 2v_\alpha o_\alpha t + o_\alpha^2) + \tau \Sigma_\alpha^2 (v_\beta^2 t^2 + 2v_\beta o_\beta t + o_\beta^2) - 2 \Sigma_\alpha^2 \Sigma_\beta^2 t \\ &= \frac{(t + a)^2 + b - a^2}{\Sigma^2} \end{aligned}$$

with the constants $a = \Sigma^2 \left(\tau \Sigma_\beta^2 v_\alpha o_\alpha + \tau \Sigma_\alpha^2 v_\beta o_\beta - \Sigma_\alpha^2 \Sigma_\beta^2 \right)$ and $b = \tau \Sigma^2 \left(\Sigma_\beta^2 o_\alpha^2 + \Sigma_\alpha^2 o_\beta^2 \right)$ and also $\Sigma^{-2} = \tau \left(\Sigma_\beta^2 v_\alpha^2 + \Sigma_\alpha^2 v_\beta^2 \right)$. Putting this t -quadratic form into the integral we obtain

$$\frac{1}{2\pi} S \frac{\sqrt{\pi \tau} \Sigma}{\sqrt{2}} \exp \left[-\frac{nT_s}{\tau} - \frac{1}{2} \frac{b - a^2}{\Sigma^2 \Sigma_\alpha^2 \Sigma_\beta^2 \tau} \right] \left(1 + \operatorname{erf} \left(\frac{nT_s + a}{\sqrt{2\tau \Sigma \Sigma_\alpha \Sigma_\beta}} \right) \right) \quad (\text{B.2})$$

where the function erf is defined by:

$$\operatorname{erf}(x) = \frac{2}{\sqrt{\pi}} \int_0^x e^{-\theta^2} d\theta = -\operatorname{erf}(-x)$$

This expression can be simplified by using the function $\operatorname{erfcx}(x) = \exp(x^2)(1 - \operatorname{erf}(x))$.

B.2. Argument of the exponential

To make the written form lighter, we can set $S = \Sigma^2 \Sigma_\alpha^2 \Sigma_\beta^2$. The factor intervening in the function exp is

$$\begin{aligned} \frac{nT_s}{\tau} - \frac{b - a^2}{2\Sigma^2 \Sigma_\alpha^2 \Sigma_\beta^2 \tau} &= -\frac{nT_s}{\tau} - \frac{b}{2S\tau} + \frac{a^2}{2S\tau} + \left(\frac{n^2 T_s^2}{2S\tau} - \frac{n^2 T_s^2}{2S\tau} \right) + \left(\frac{2nT_s a}{2S\tau} - \frac{2nT_s a}{2S\tau} \right) \\ &= -\frac{nT_s}{\tau} - \frac{b}{2S\tau} - \frac{2nT_s a}{2S\tau} - \frac{n^2 T_s^2}{2S\tau} + \left(\frac{nT_s + a}{\sqrt{2S\tau}} \right)^2 \end{aligned}$$

So, by injecting this expression in (B.2), the function erfcx appears

$$\begin{aligned} \exp \left[-\frac{nT_s}{\tau} - \frac{b - a^2}{2S\tau} \right] \left(1 + \operatorname{erf} \left(\frac{nT_s + a}{\sqrt{2S\tau}} \right) \right) &= \\ \exp \left[-\frac{nT_s}{\tau} - \frac{b}{2S\tau} - \frac{2nT_s a}{2S\tau} - \frac{n^2 T_s^2}{2S\tau} \right] \operatorname{erfcx} \left(-\frac{nT_s + a}{\sqrt{2S\tau}} \right). \end{aligned}$$

The values of S , a and b can be replaced. First of all, the argument of the exponential is written

$$\begin{aligned} -\frac{nT_s}{\tau} - \frac{\tau \Sigma^2 (\Sigma_\beta^2 o_\alpha^2 + \Sigma_\alpha^2 o_\beta^2)}{2\Sigma^2 \Sigma_\alpha^2 \Sigma_\beta^2 \tau} - \frac{2nT_s \Sigma^2 (\tau \Sigma_\beta^2 v_\alpha o_\alpha + \tau \Sigma_\alpha^2 v_\beta o_\beta - \Sigma_\alpha^2 \Sigma_\beta^2)}{2\Sigma^2 \Sigma_\alpha^2 \Sigma_\beta^2 \tau} - \frac{n^2 T_s^2}{2S\tau} &= \\ -\frac{nT_s}{\tau} - \frac{o_\alpha^2}{2\Sigma_\alpha^2} - \frac{o_\beta^2}{2\Sigma_\beta^2} - \frac{2nT_s v_\alpha o_\alpha}{2\Sigma_\alpha^2} - \frac{2nT_s v_\beta o_\beta}{2\Sigma_\beta^2} + \frac{nT_s}{\tau} - \frac{n^2 T_s^2}{2\Sigma^2 \Sigma_\alpha^2 \Sigma_\beta^2 \tau}, \quad (\text{B.3}) \end{aligned}$$

and the terms nT_s/τ simplify. We then use the expression for Σ^2

$$\frac{n^2 T_s^2}{2\Sigma^2 \Sigma_\alpha^2 \Sigma_\beta^2 \tau} = \frac{n^2 T_s^2 \tau (\Sigma_\beta^2 v_\alpha^2 + \Sigma_\alpha^2 v_\beta^2)}{2\Sigma_\alpha^2 \Sigma_\beta^2 \tau} = \frac{n^2 T_s^2 v_\alpha^2}{2\Sigma_\alpha^2} + \frac{n^2 T_s^2 v_\beta^2}{2\Sigma_\beta^2},$$

to bring out two perfect squares. Finally the argument of the exponential (B.3) in (B.2) is written

$$-\frac{(o_\alpha + nT_s v_\alpha)^2}{2\Sigma_\alpha^2} - \frac{(o_\beta + nT_s v_\beta)^2}{2\Sigma_\beta^2} \quad (\text{B.4})$$

which is exactly the argument of a bivariate Gaussian. We again find the same standard deviations Σ_α and Σ_β . However, the response of the optics, initially (o_α, o_β) , is now shifted by $(nT_s v_\alpha, nT_s v_\beta)$, i.e. the pointing difference between two successive time samples.

B.3. Argument of the function erfcx and final expression

Another term is needed if we are to know the global response. It comes from the function erfcx, which corresponds to the influence of the bolometer. The argument of the function erfcx is

$$\begin{aligned} -\frac{nT_s + a}{\sqrt{2\tau \Sigma \Sigma_\alpha \Sigma_\beta}} &= -\frac{nT_s + \Sigma^2 (\tau \Sigma_\beta^2 v_\alpha o_\alpha + \tau \Sigma_\alpha^2 v_\beta o_\beta - \Sigma_\alpha^2 \Sigma_\beta^2)}{\sqrt{2\tau \Sigma \Sigma_\alpha \Sigma_\beta}} \\ &= \frac{\Sigma_\alpha \Sigma_\beta}{\sqrt{2\tau \Sigma_v}} - \frac{\Sigma_\beta v_\alpha (o_\alpha + nT_s v_\alpha)}{\sqrt{2\Sigma_\alpha \Sigma_v}} - \frac{\Sigma_\alpha v_\beta (o_\beta + nT_s v_\beta)}{\sqrt{2\Sigma_\beta \Sigma_v}} \quad (\text{B.5}) \end{aligned}$$

where $\Sigma_v^2 = \Sigma_\beta^2 v_\alpha^2 + \Sigma_\alpha^2 v_\beta^2$ and what is of interest here is that the same factors are found in the argument of the exponential. To know the global response, we need to bring everything together. By injecting the expressions of

the arguments (B.4) and (B.5), we obtain

$$\begin{aligned} \frac{1}{2\pi} S \frac{\sqrt{\pi\tau\Sigma}}{\sqrt{2}} \exp \left[\frac{nT_s}{\tau} - \frac{1}{2} \frac{b - a^2}{\Sigma^2 \Sigma_\alpha^2 \Sigma_\beta^2 \tau} \right] \left(1 + \operatorname{erf} \left(\frac{nT_s + a}{\sqrt{2\tau\Sigma\Sigma_\alpha\Sigma_\beta}} \right) \right) = \\ \frac{S}{2\sqrt{2\pi\Sigma_v}} \exp \left[-\frac{(o_\alpha + nT_s v_\alpha)^2}{2\Sigma_\alpha^2} - \frac{(o_\beta + nT_s v_\beta)^2}{2\Sigma_\beta^2} \right] \\ \operatorname{erfcx} \left(\frac{\Sigma_\alpha \Sigma_\beta}{\sqrt{2\tau\Sigma_v}} - \frac{\Sigma_\beta v_\alpha (o_\alpha + nT_s v_\alpha)}{\sqrt{2\Sigma_\alpha \Sigma_v}} - \frac{\Sigma_\alpha v_\beta (o_\beta + nT_s v_\beta)}{\sqrt{2\Sigma_\beta \Sigma_v}} \right) \quad (\text{B.6}) \end{aligned}$$

with, similarly for α and β : $\Sigma_{\alpha/\beta}^2 = \sigma_{\alpha/\beta}^2 + \sigma_o^2$, which finishes the integration of (13) over time.

Appendix C: Direct model computation algorithm

This part gives some more details on the concrete calculation of a model output $\mathbf{H}\mathbf{x}$ of Section 2.3. First of all, there are four different impulse responses whatever the number of scans. For two scans in the same direction, the convolution is the same. Thus we can construct four different convolution matrices \mathbf{H}_i for $i = 1, 2, 3, 4$ and apply four different discrete convolutions to the coefficients \mathbf{x} .

We can also deduce the structure of the transpose of the model $\mathbf{H}^t = \mathbf{H}_c^t \mathbf{P}^t$. The matrix \mathbf{P}^t is a data summation / zero fill matrix (addition of the data that possess the same pointing while setting the other coefficients to zero), and \mathbf{H}_c^t corresponds to a convolution with the space reversal impulse responses.

The product by \mathbf{P}^t is very similar to the construction of a naive map except that the data are added rather than averaged. Also, the operation is done by velocity and not globally. Finally, the products by \mathbf{H}_c and \mathbf{H}_c^t are convolutions implemented by FFT.

References

- Abergel, A., Arab, H., Compiègne, M., et al. 2010, A&A, 518, L96+
- Andrews, H. C. & Hunt, B. R. 1977, Digital Image Restoration (Englewood Cliffs, NJ: Prentice-Hall)
- Boulanger, F., Abergel, A., Bernard, J., et al. 1996, A&A, 312, 256
- Cantalupo, C. M., Borrill, J. D., Jaffe, A. H., Kisner, T. S., & Stompor, R. 2010, The Astrophysical Journal Supplement, 187, 212
- Champagnat, F., Le Besnerais, G., & Kulcsár, C. 2009, Journal of the Optical Society of America A, 26, 1730
- Charbonnier, P., Blanc-Féraud, L., Aubert, G., & Barlaud, M. 1997, IEEE Trans. Image Processing, 6, 298
- Clements, D., Chaniel, P., Bendo, G., et al. 2006, SPIRE Mapmaking Algorithm Review Report, Tech. rep., Astrophysics group at Imperial College London
- de Graauw, T., Helmich, F. P., Phillips, T. G., et al. 2010, A&A, 518, L6+
- Demoment, G. 1989, IEEE Trans. Acoust. Speech, Signal Processing, ASSP-37, 2024
- Elad, M. & Feuer, A. 1999, IEEE Trans. Image Processing, 8, 387
- Farsiu, S., Robinson, M., Elad, M., & Milanfar, P. 2004, Image Processing, IEEE Transactions on, 13, 1327
- Ferlet, M. 2007, Spire calibration files: Photometer beam profiles, Tech. rep., University of Wales Cardiff

- Griffin, M., Swinyard, B., Vigroux, L., et al. 2008, in Presented at the Society of Photo-Optical Instrumentation Engineers (SPIE) Conference, Vol. 7010, Society of Photo-Optical Instrumentation Engineers (SPIE) Conference Series
- Griffin, M. J. 2006, Revised Photometer sensitivity model, working version after sensitivity review meeting
- . 2007, The SPIRE Analogue Signal Chain and Photometer Detector Data Processing Pipeline, Tech. rep., University of Wales Cardiff
- Griffin, M. J., Abergel, A., Abreu, A., et al. 2010, *A&A*, 518, L3+
- Griffin, M. J., Bock, J. J., & Gear, W. K. 2002, *Applied Optics*, 41, 6543
- Hansen, P., Jacobsen, M., Rasmussen, J., & Sørensen, H. 2000, in *Methods and Applications of Inversion*, Lecture Notes in Earth Sciences, ed. P. Hansen, B. Jacobsen, & K. Mosegaard, Vol. 92 (Berlin: Springer)
- Hardie, R. C., Barnard, K. J., & Armstrong, E. E. 1997, *IEEE Trans. Image Processing*, 6, 1621
- Idier, J., ed. 2008, *Bayesian Approach to Inverse Problems* (London: ISTE Ltd and John Wiley & Sons Inc.)
- Künsch, H. R. 1994, *Ann. Inst. Stat. Math.*, 46, 1
- Leshem, A., Christou, J., Jeffs, B. D., Kuruoglu, E., & van der Veen, A. J. 2008, *IEEE Journal of Selected Topics in Signal Processing*, 2
- Leshem, A., Kamalabadi, F., Kuruoglu, E., & van der Veen, A.-J. 2010, *Signal Processing Magazine*, 27
- Miville-Deschênes, M., Martin, P. G., Abergel, A., et al. 2010, *A&A*, 518, L104+
- Molina, R. & Ripley, B. D. 1989, *J. Appl. Statistics*, 16, 193
- Nguyen, N., Milanfar, P., & Golub, G. 2001, *IEEE Trans. Image Processing*, 10, 573
- Nocedal, J. & Wright, S. J. 2000, *Numerical Optimization*, Series in Operations Research (New York: Springer Verlag)
- Orieux, F. 2009, PhD thesis, Université Paris-Sud 11
- . 2010, Materials of aa1.
- Orieux, F., Giovannelli, J.-F., & Rodet, T. 2010, *J. Opt. Soc. Am. A*, 27, 1593
- Orieux, F., Rodet, T., & Giovannelli, J.-F. 2009, in *Proc. of IEEE International Conference on Image Processing (ICIP 2009)*, Cairo, Egypt
- Park, S. C., Park, M. K., & Kang, M. G. 2003, *IEEE Trans. Signal Processing Mag.*, 21
- Patanchon, G., Ade, P. A. R., Bock, J. J., et al. 2008, *The Astrophysical Journal*, 681, 708
- Patti, A. J., Sezan, M. I., & Tekalp, A. M. 1997, *IEEE Trans. Image Processing*, 6, 1064
- Pilbratt, G. L., Riedinger, J. R., Passvogel, T., et al. 2010, *A&A*, 518, L1+
- Poglitsch, A., Waelkens, C., Geis, N., et al. 2010, *A&A*, 518, L2+
- Richardson, W. H. 1972, *J. Opt. Soc. Amer.*, 62, 55
- Rocheftort, G., Champagnat, F., Le Besnerais, G., & Giovannelli, J.-F. 2006, *IEEE Trans. Image Processing*, 15, 3325
- Rodet, T., Orieux, F., Giovannelli, J.-F., & Abergel, A. 2008, *IEEE J. of Selec. Topics in Signal Proc.*, 2, 802
- Shannon, C. E. & Weaver, W. 1948, *Bell Syst. Tech. J.*, 27, 379
- Shewchuk, J. R. 1994, *An Introduction to the Conjugate Gradient Method Without the Agonizing Pain*, Tech. rep., Carnegie Mellon University
- Sibthorpe, B., Chanial, P., & Griffin, M. J. 2009, ArXiv e-prints

- Sibthorpe, B. & Griffin, M. J. 2006, Spire Photometer Simulator, Tech. rep., University of Wales Cardiff
- Sudiwala, R. V., Griffin, M. J., & Woodcraft, A. L. 2002, *International Journal of Infrared and Millimeter Waves*, 23, 545
- Tikhonov, A. & Arsenin, V. 1977, *Solutions of Ill-Posed Problems* (Washington, DC: Winston)
- Twomey, S. 1962, *J. Assoc. Comp. Mach.*, 10, 97
- Vandewalle, P., Sbaiz, L., Vandewalle, J., & Vetterli, M. 2007, *IEEE Trans. Signal Processing*, 55, 3687
- Wieprecht, E., Schreiber, J., de Jong, J., et al. 2009, in *Astronomical Society of the Pacific Conference Series*, Vol. 411, *Astronomical Society of the Pacific Conference Series*, ed. D. A. Bohlender, D. Durand, & P. Dowler, 531–+
- Woods, N. A., Galatsanos, N. P., & Katsaggelos, A. K. 2006, *IEEE Trans. Image Processing*, 15, 201